ChemComm

COMMUNICATION

View Article Online
View Journal | View Issue



Cite this: *Chem. Commun.*, 2025, **61**, 18436

Received 22nd August 2025,
Accepted 16th October 2025

DOI: 10.1039/d5cc04773k

rsc.li/chemcomm



# Rapid solvent-free synthesis of Ga-doped LLZO ($Li_{5.5}Ga_{0.5}La_3Zr_2O_{12}$): towards scalable garnet electrolyte for next generation solid-state batteries

Rahul Rajeev, Abhaya Kumar Mishra and Kyle S. Brinkman *

**Gallium (Ga) doping in the LLZO family is a well-known strategy for achieving high lithium-ion conductivity. Here, we report a one-step solvent-free combustion synthesis of 0.5 atom per formula unit (p.f.u.) Ga-doped cubic phase LLZO within 15 minutes. The LLZO pellet sintered at 1100 °C for 5 h exhibits a total Li-ion conductivity of 5.8 × $10^{-4}$ S $cm^{-1}$ with an activation energy of 0.3 eV, comparable to existing state-of-the-art processes.**

Rechargeable lithium-ion batteries (LIBs) are promising electrochemical energy-storage systems for the green industrial economy and transportation electrification.[1,2] Organic liquid electrolytes commonly employed in LIBs are associated with numerous challenges, particularly leakage and flammability, which pose safety concerns.[3,4] Moreover, the liquid electrolytes exhibit poor compatibility with lithium-metal anodes (3860 mA h $g^{-1}$) and high-voltage cathodes, thus failing to meet the requirements for future energy storage demands.[5,6] Replacing the liquid with solid-state electrolytes, functioning as a separator, is expected to address these fundamental challenges.[7,8] Since the report by Murugan *et al.* in 2007, lithium-stuffed inorganic garnet LLZO has been extensively explored for next-generation LIBs.[9,10] Li-ion conductivity in LLZO is primarily governed by its phase purity, crystal structure and relative density (RD) of sintered material.[11,12] Recently, Anderson *et al.* reported that among available dopants, gallium ($Ga^{3+}$) doping at lithium sites significantly enhances ionic conductivity.[13] The impacts of Ga doping could be understood with the Kröger–Vink notation, $Ga_2O_3 + Li_2O \rightarrow 2Ga_{Li}^{\bullet\bullet} + 4O_O^{\times} + 4V'_{Li}$. Therefore, it is believed that the formation of Li vacancies, electrostatic repulsion, and structural shifts together enhance the ionic conductivity.[14] However, Ga-stabilized cubic phase LLZO (c-GaLLZO) electrolytes still face serious challenges related to materials processing (Table S1, SI) and stable electrolyte–electrode interfaces.[15]

As illustrated in Table S1 (SI), the conventional solid-state method necessitates extended periods of intensive milling, high temperature calcination (900–1100 °C), and excess Li sources to prevent $La_2Zr_2O_7$ (LZO) formation. This results in micron-sized aggregate particles, significantly impeding densification of the material. Wet chemical routes such as sol–gel,[16] Pechini,[17] and co-precipitation[18] yield nanosized LLZO particles at low temperatures.[19] However, the use of toxic reagents and multistep processing raises overall materials costs. Thus, simple, cost-effective synthesis of nanostructured c-GaLLZO is essential to bridge the gap between lab-scale research and industrial applications.

To overcome the aforementioned challenges, in the present study, a facile single-step solvent-free combustion method was employed to prepare cubic phase Ga-LLZO (c-GaLLZO). c-GaLLZO was synthesized *via* solvent-free, urea-assisted combustion of metal nitrates (0.5 p.f.u Ga at Li site and 10% excess Li) for 15 minutes in a preheated furnace, and the detailed synthesis method is described in the SI and the process is shown schematically in Fig. 1a. To understand the formation mechanism, the intermediate products were collected at intervals of 150 °C from room temperature to 750 °C and characterized using XRD (Fig. 1b). The mixture of nitrate-bonded cations with urea shows broadened peaks, indicating homogeneous mixing and close proximity of ions within the complex. The reduced number of peaks in the XRD patterns of the intermediate samples collected at 150 and 300 °C confirms the atomic rearrangement to reduce structural disorder. At 450 °C, a hump at $2\theta$ = 25–35° in the XRD pattern suggests an intermediate amorphous phase. The product formed at 600 °C matches $La_2Zr_2O_7$ (LZO) (ICDD card number 73-0444).[20] Kong *et al.* reported the formation of an amorphous intermediate before crystalline LZO.[21] At 750 °C, the LZO transformed into c-GaLLZO. FTIR spectra (Fig. 1c) confirm the precursor mixture-urea complex formation; urea bands are at 1678 $cm^{-1}$ and 3429 $cm^{-1}$, corresponding to carbonyl (C═O) and N–H stretching modified in the complex, with C═O frequency shift towards a lower wavenumber indicating metal coordinate bonding (C═O → M). Fig. 1d shows the TGA and DSC curves of the representative sample with fuel to oxidizer ratio (F/O) = 0.5, highlighting three major regions of weight loss. The first weight loss at 120 °C in the TGA curve associated with an endothermic peak in DSC corresponds to mixed-nitrate

*Department of Materials Science and Engineering, Clemson University, Clemson, SC-29634, USA. E-mail: ksbrink@clemson.edu*

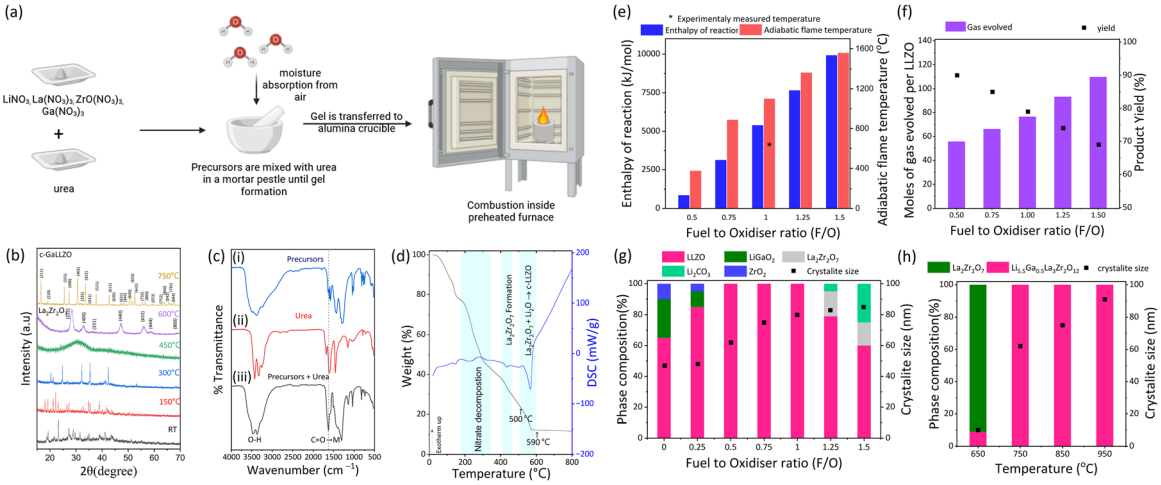


Fig. 1 (a) Schematic illustration of LLZO processing (Created with BioRender.com). (b) XRD pattern of samples calcined at various temperatures. (c) FTIR spectra of (i) the precursor mixture, (ii) urea, and (iii) the precursor mixture-urea composite, and (d) TGA/DSC profile of the precursor mixture-urea composite at F/O = 0.5. Influence of F/O ratio on (e) the enthalpy of reaction and the corresponding experimental and associated adiabatic flame temperature, and (f) the volume of gas evolved together with the product yield. Histogram of phase composition (%), and crystallite size as a function of (g) F/O, and (h) temperature.

dehydration. The second weight loss step corresponds to decomposition of nitrate bound cations in the temperature range of 200 °C to 450 °C, forming LZO, supported by a hump in the XRD data, indicating LZO formation from nitrate-bound metal ion(s). The third weight loss step (500–590 °C) arises from lithium nitrate decomposition, where intermediate product $Li_2O$ combined with LZO to form LLZO. After heating to 800 °C no weight loss was observed, indicating no further phase transformation.

The thermodynamic aspect of F/O is essential to optimize metal–fuel complexes (the equation and detailed explanation are shown in eqn S2 and S3, SI) to achieve structural integrity and maximum yield. An increase in the calculated ($\Delta H_r^o$), and ($T_{ad}$) was observed moving from fuel-lean (F/O < 1) to fuel-rich (F/O > 1) conditions (Fig. 1e). However, the maximum temperature of 650 °C was achieved at F/O = 1. A white, fluffy mass was obtained at F/O = 0.5 with a maximum powder yield of 90%. Increasing the F/O ratio to 0.75, 1, 1.25, and 1.5 resulted in a lower product yield of 87%, 83%, 77%, and 71%, respectively, which may be due to the release of a large volume of gaseous species (Fig. 1f), causing the solid powder to spill over. Rietveld-refined diffraction patterns of the powder obtained under various experimental conditions such as different F/O and temperature are shown in Fig. S1 and S2 (SI). Phase composition and crystallite size (Halder–Wagner method) *versus* F/O are presented in Fig. 1g. Samples without urea showed maximum impurities, while fuel-lean (0.5, 0.75) and stoichiometric (1) ratios yielded cubic LLZO. Crystallite size increased with F/O, with the smallest (62.1 nm) at 0.5. However, unreacted residues such as $Li_2CO_3$ and $La_2Zr_2O_7$ were seen for the fuel-rich state (1.25 and 1.5), possibly due to the temperature drop at the time of reaction caused by gas evolution. The effect of temperature (preheated furnaces) was also investigated while maintaining other experimental parameters such as F/O = 0.5 and reaction duration 15 min, respectively. The histogram (Fig. 1h) depicts the phase composition and crystalline sizes as a function of temperature, revealing the formation of the $La_2Zr_2O_7$ phase at 650 °C.

Fig. 2 shows the FE-SEM images of LLZO powder calcined at (a) 750 °C, (c) 850 °C, and (d) 950 °C for 15 minutes, while maintaining F/O = 0.5. At 750 °C (Fig. 2a), LLZO exhibits mixed morphologies comprising spherical particles (190 nm) and ligamentous structures (140 nm). Badami *et al.* reported similar mixed morphologies for Al-doped LLZO.[22] Elemental mapping confirms uniform distribution of La, Zr, Ga, and O throughout the samples, suggesting no cluster formation and corroborating the XRD data. However, on increasing temperature to 850 °C, the particles become less spherical, and the ligamentous structures become thicker (320 nm) with lower porosity (Fig. 2c). At 950 °C (Fig. 2d), the morphology changes to entirely ligamentous

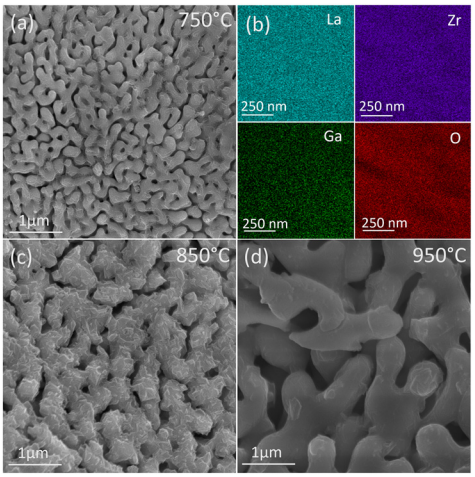


Fig. 2 FE-SEM images of c-GaLLZO prepared from the precursor mixture-urea composite (F/O = 0.5), calcined at different temperatures for 15 minutes: (a) 750 °C and its corresponding energy-dispersive X-ray (EDX) mapping in (b), (c) 850 °C and (d) 950 °C.

structures (560 nm), indicating a pivotal role of temperature in shaping the microstructure of c-GaLLZO. The low calcination temperature favors the formation of smaller particles associated with high surface energies suitable for sintering, whereas higher temperature promotes particle coarsening, resulting in a thicker ligamentous structure. The morphologies at F/O ratios of 0.75 and 1 (Fig. S3a and b, SI) were found to be similar to that at an F/O ratio of 0.5 (Fig. 2a). However, the average width of the ligamentous structures increased to 248 nm and 300 nm for F/O = 0.75 and 1, respectively (Table S3, SI). Under fuel-rich conditions (F/O = 1.25 and 1.5; Fig. S3c and d, SI) irregular shaped particles along with cavities were observed. This underscores that gas evolution likely displaces particles during combustion.

c-GaLLZO calcined at 750 °C for 15 minutes with a smaller particle size (Fig. 2a) was fabricated into green pellets to enhance densification; it comprised irregularly packed particles with an RD of 62% (Fig. S4, SI). At 950 °C for 5 h the sintered pellet exhibits a porous structure with loosely connected grains and an RD of 80% (Fig. S5a-a1, SI), underscoring that low-temperature sintering, enabled by smaller particles, promotes shortened diffusion paths. The pellet sintered at 1000 °C consists of spherical particles with rough surfaces and visible pores (Fig. S5b-b1, SI). Upon closer observation, the grain necking is evident, driven by surface diffusion due to surface energy. The histogram of the particle size shown in Fig. S5b2 (SI) indicates an asymmetric distribution with average particle size of 3.94 μm, with an RD of 88%. Interestingly, loosely packed polyhedral grains with reduced porosity and a moderately rough surface were observed for the pellet sintered at 1050 °C (Fig. 3a-a1). The average grain size (Fig. 3a) and RD were 5.13 μm and 91.5%, respectively. The above results underscore the improvement in LLZO pellet densification with temperature, attributed to increased surface and grain boundary diffusion coefficients at elevated temperatures.[23] At 1100 °C, the green pellet reached its optimal sintering temperature, resulting in well-defined, tightly connected smooth polyhedral grains, suggesting near-complete densification (Fig. 3b-b1). The presence of larger grains suggests fewer grain boundaries, which facilitates faster Li-ion transport. The pellet attained an RD of 94.2% and exhibited a narrow Gaussian grain size distribution, with an average grain size of 7.51 μm. These features further indicate progressive pore shrinkage and effective necking between particles. In contrast, elevating the sintering temperature to 1150 °C and 1200 °C led to a rougher surface along with abnormal grain growth, as evident from Fig. 3c-c1, and Fig. S5c-c2 (SI), respectively. The sintered pellet exhibited an average grain size of 8.4 μm (RD = 95.1%) and 9 μm (RD = 95.5%) at 1150 °C and 1200 °C, respectively.

High-angle annular dark field scanning transmission electron microscopy (HAADF-STEM) and high-resolution transmission electron microscopy (HRTEM) images were acquired to assess the structural stability of the optimized sintered pellet prepared at 1100 °C, for 5 h (Fig. 3d–f). The HAADF-STEM images of a single grain (Fig. 3d) display uniform contrast, indicating that the constituent elements are present all over the grain, as image contrast is directly proportional to atomic number of the element. The elemental mapping (Fig. 3e) indicates a uniform distribution of La, Zr, Ga, and O throughout the grain. Fig. 3f shows the high-resolution TEM images, which confirm the crystalline nature, where the lattice fringe spacing of 0.53 nm corresponds to the {112} plane, further supporting the cubic phase stabilized LLZO. The observed lattice spacing value is comparable to that reported by Huang *et al.* for Ga doped LLZO.[24]

Electrochemical impedance spectroscopy (EIS) measurements were performed using Li|LLZO|Li symmetric cells to evaluate and compare the Li-ion conductivity of sintered c-GaLLZO. An equivalent circuit model (inset in Fig. 3g) comprising resistors (R) and constant phase elements (CPEs) is utilized to fit the Nyquist plots.[25] The subscripts b, gb, and el indicate

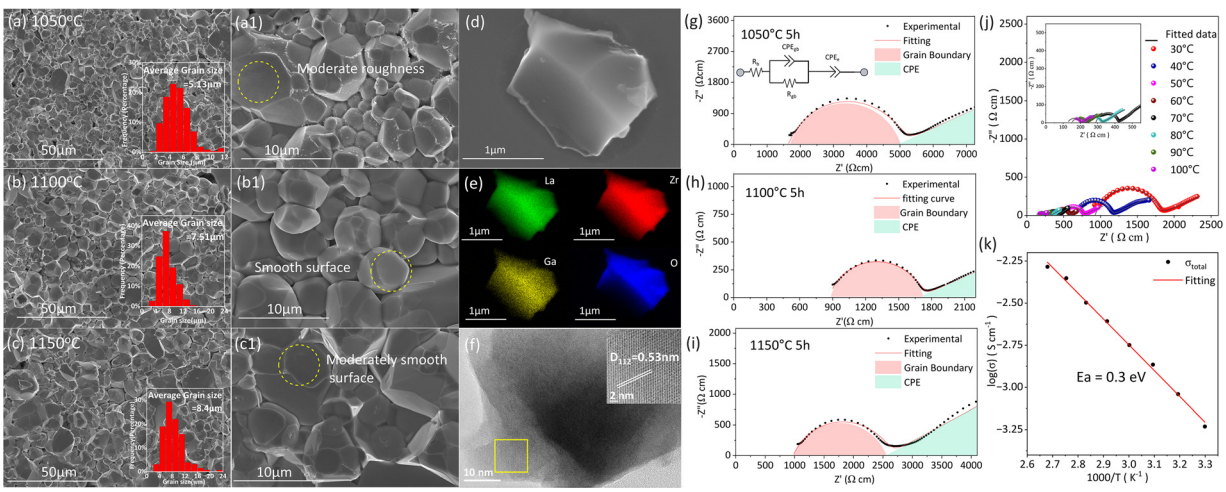


Fig. 3 (a)–(c) FE-SEM images of the c-GaLLZO pellets sintered at (a, a1) 1050 °C, (b, b1) 1100 °C and (c, c1) 1150 °C. (d) HAADF-STEM, (e) EDX mapping and (f) HRTEM image of the pellet sintered at 1100 °C. (g)–(i) Nyquist plots of Li|LLZO|Li symmetric cells presented at (g) 1050 °C, (h) 1100 °C, and (i) 1150 °C. (j) and (k) show the (j) temperature dependent Nyquist plot and (k) Arrhenius plot of total ionic conductivity of the 1100 °C pellet. Insets in (a)–(c) show the corresponding particle size distribution, and (f) includes the HRTEM images and (g) equivalent circuit.

 

the bulk, grain, and charge transfer resistance, respectively. Fig. 3g–i depicts the normalized Nyquist plots collected at 30 °C for LLZO pellets sintered at 1050 °C, 1100 °C, and 1150 °C. The total conductivity values ($\sigma_t$) were calculated using the following formula $\sigma_t = l/(R_t S)$; here, $l$ represents the pellet thickness, $S$ is the electrode surface area, and $R_t = R_b + R_{gb}$, denotes total resistance. The highest total ionic conductivity ($5.8 \times 10^{-4}$ S cm$^{-1}$) was obtained for the pellet sintered at 1100 °C, which is attributed to its high RD of 94.2%, uniform grain size, and tight contact between grain boundaries (Fig. 3b-b1, Table S4, SI). The highest ionic conductivity is comparable with other c-GaLLZO materials synthesized by solid-state methods and chemical routes (Table S1, SI). The lower ionic conductivity of $2 \times 10^{-4}$ S cm$^{-1}$ found for the pellet sintered at 1050 °C may be due to the presence of a larger number of grain boundaries and lower density. Increasing the sintering temperature from 1100 °C to 1150 °C decreased the total conductivity to $4 \times 10^{-4}$ S cm$^{-1}$. On closer observation, we found that the pellet sintered at 1150 °C exhibits higher grain boundary resistance, possibly due to lithium loss and abnormal grain growth. However, no LZO phase impurities were observed in the XRD data for these sintered pellets (Fig. S6, SI).

The temperature dependent EIS analysis was performed for the representative c-GaLLZO pellets exhibiting the highest Li-ion conductivity. As shown in Fig. 3j, the size of the semicircle in the Nyquist plot decreases and becomes less prominent with increasing temperature, suggesting reduced impedance due to thermally activated conduction. The activation energy of the pellet was measured by the Arrhenius law $\sigma_t = Ae\hat{}(-E_a/RT)$, where $E_a$ represents the activation energy, $A$ indicates the pre-exponential factor, $T$ is the absolute temperature in Kelvin, $R$ is the universal gas constant and $\sigma_t$ is the total conductivity. The observed activation energy of 0.3 eV (Fig. 3k) is consistent with the values reported in the literature.[26]

In summary, we demonstrated a rapid, solvent-free combustion method to prepare c-GaLLZO in only 15 minutes. This method uses only precursor salts and urea, making the synthesis process reliable, scalable, and highly desirable for industrial applications. The final pellet, sintered at 1100 °C for 5 h, delivered high ionic conductivity of $5.8 \times 10^{-4}$ S cm$^{-1}$ with a low 0.3 eV activation energy. The F/O ratio plays a pivotal role; notably, even using half the fuel calculated from the stoichiometric requirement produced uniform small c-GaLLZO with maximal product yield. This work bypasses traditional high-cost synthesis routes while producing a superior solid electrolyte, offering a valuable pathway for material fabrication towards solid-state battery technology.

This project was funded the US DOE Advanced Research Projects Agency – Energy (ARPAa-E) Award Number DEAR0001375.

## Conflicts of interest

There are no conflicts to declare.

## Note added after first publication

This article replaces the version published on 28 October 2025, where parts of Fig. 1 were missing.

## Data availability

All data supporting this article are available in the supplementary information (SI). Supplementary information includes experimental methods, characterization (XRD, SEM, TEM, FTIR, TGA/DSC, EIS), thermodynamic F/O analyses, and supporting figures/tables. See DOI: **https://doi.org/10.1039/d5cc04773k**.

## Notes and references

1 P. Greim, A. A. Solomon and C. Breyer, *Nat. Commun.*, 2020, **11**, 4570.
2 F. Xie, Y. Deng, Y. Xie, H. Xu and G. Chen, *Chem. Commun.*, 2015, **51**, 3545.
3 Z. Gao, H. Sun, L. Fu, F. Ye, Y. Zhang, W. Luo and Y. Huang, *Adv. Mater.*, 2018, **30**, 1705702.
4 C. Yang, Z. Jiang, X. Chen, W. Luo, T. Zhou and J. Yang, *Chem. Commun.*, 2024, **60**, 10245.
5 J. F. Wu, B. W. Pu, D. Wang, S. Q. Shi, N. Zhao, X. Guo and X. Guo, *ACS Appl. Mater. Interfaces*, 2019, **11**, 898–905.
6 V. Rajsundar, C. J. Kiruthik Pranav, S. Karuppasamy and A. M. Stephan, *Chem. Commun.*, 2025, **61**, 12618–12642.
7 S. A. Jose, A. Gallant, P. L. Gomez, Z. Jaggers, E. Johansson, Z. LaPierre and P. L. Menezes, *Batteries*, 2025, **11**, 90.
8 H. Xie, Z. Yang, J. Liu, W. Wu, T. Huang and H. Liu, *Chem. Commun.*, 2025, **61**, 10449–10469.
9 R. Murugan, V. Thangadurai and W. Weppner, *Angew. Chem., Int. Ed.*, 2007, **46**, 7778–7781.
10 C. Wang, K. Fu, S. P. Kammampata, D. W. McOwen, A. J. Samson, L. Zhang, G. T. Hitz, A. M. Nolan, E. D. Wachsman, Y. Mo, V. Thangadurai and L. Hu, *Chem. Rev.*, 2020, **120**, 4257–4300.
11 M. S. Diallo, T. Shi, Y. Zhang, X. Peng, I. Shozib, Y. Wang, L. J. Miara, M. C. Scott, Q. H. Tu and G. Ceder, *Nat. Commun.*, 2024, **15**, 858.
12 E. J. Cussen, *J. Mater. Chem.*, 2010, **20**, 5167–5173.
13 E. Anderson, E. Zolfaghar, A. Jonderian, R. Z. Khaliullin and E. McCalla, *Adv. Energy Mater.*, 2024, **14**, 2304025.
14 N. Birkner, C. Li, S. L. Estes and K. S. Brinkman, *ChemSusChem*, 2021, **14**, 2621–2630.
15 J. Minkiewicz, G. M. Jones, S. Ghanizadeh, S. Bostanchi, T. J. Wasely, S. A. Yamini and V. Nekouie, *Open Ceram.*, 2023, **16**, 100497.
16 I. Kokal, M. Somer, P. H. L. Notten and H. T. Hintzen, *Solid State Ion.*, 2011, **185**, 42–46.
17 S. Afyon, F. Krumeich and J. L. M. Rupp, *J. Mater. Chem. A*, 2015, **3**, 18636–18648.
18 C. Shao, H. Liu, Z. Yu, Z. Zheng, N. Sun and C. Diao, *Solid State Ion.*, 2016, **287**, 13–16.
19 G. Kalita, T. Endo and T. Nishi, *J. Alloys Compd.*, 2023, **969**, 172281.
20 H. Chen, Y. Wang, J. Su, L. Yang and H. Bai, *Inorg. Chem.*, 2023, **62**, 4558–4569.
21 L. Kong, I. Karatchevtseva, D. J. Gregg, M. G. Blackford, R. Holmes and G. Triani, *J. Am. Ceram. Soc.*, 2013, **96**, 935–941.
22 P. Badami, S. Smetaczek, A. Limbeck, D. Rettenwander, C. K. Chan and A. N. M. Kannan, *Mater. Adv.*, 2021, **2**, 5181–5188.
23 C. Li, Y. Liu, J. He and K. S. Brinkman, *J. Alloys Compd.*, 2017, **695**, 3744–3752.
24 C. Y. Huang, Y. T. Tseng, H. Y. Lo, J. K. Chang and W. W. Wu, *Nano Energy*, 2020, **71**, 104625.
25 R. H. Lee, C. Y. Kang, J. K. Lee, B. S. Jin, K. N. Kim, H. S. Kim, J. R. Yoon and S. H. Lee, *NPG Asia Mater.*, 2024, **16**, 42.
26 C. Bernuy-Lopez, W. Manalastas, J. M. Lopez Del Amo, A. Aguadero, F. Aguesse and J. A. Kilner, *Chem. Mater.*, 2014, **26**, 3610–3617.